ORIGINAL ARTICLE





Simulation-Informed Power Budget Estimate of a Fully-Implantable Brain–Computer Interface

Claudia Serrano-Amenos¹ • Frank Hu² · Po T. Wang¹ · Payam Heydari³ · An H. Do⁴ · Zoran Nenadic¹

Received: 8 May 2023 / Accepted: 28 April 2024 / Published online: 16 May 2024 © The Author(s) under exclusive licence to Biomedical Engineering Society 2024

Abstract

This study aims to estimate the maximum power consumption that guarantees a thermally safe operation for a titanium-enclosed chest wall unit (CWU) subcutaneously implanted in the pre-pectoral area. This unit is a central piece of an envisioned fully-implantable bi-directional brain-computer interface (BD-BCI). To this end, we created a thermal simulation model using the finite element method implemented in COMSOL. We also performed a sensitivity analysis to ensure that our predictions were robust against the natural variation of physiological and environmental parameters. Based on this analysis, we predict that the CWU can consume between 378 and 538 mW of power without raising the surrounding tissue's temperature above the thermal safety threshold of 2 °C. This power budget should be sufficient to power all of the CWU's basic functionalities, which include training the decoder, online decoding, wireless data transmission, and cortical stimulation. This power budget assessment provides an important specification for the design of a CWU—an integral part of a fully-implantable BD-BCI system.

 $\textbf{Keywords} \ \ Brain-computer interface \ (BCI) \cdot Electrocorticography \ (ECoG) \cdot Chest \ wall \ unit \ (CWU) \cdot Finite \ element \ method \ (FEM)$

Introduction

RECENT technological advancements have led to significant improvements in implantable medical technology and have spurred the development of novel active implantable devices. These systems are crucial in tackling medical conditions for which pharmacological or surgical approaches are deemed inadequate. Examples include next-generation pacemakers [1], implantable cardioverter-defibrillators [2], vagus nerve stimulators [3], deep brain stimulators (DBS)

Associate Editor Stefan M. Duma oversaw the review of this article.

- ☐ Claudia Serrano-Amenos clauds3@uci.edu
- Department of Biomedical Engineering, UCI, Irvine, CA 92697, USA
- Department of Mechanical and Aerospace Engineering, UCI, Irvine, CA 92697, USA
- Department of Electrical Engineering and Computer Science, UCI, Irvine, CA 92697, USA
- Department of Neurology, UCI, Irvine, CA 92697, USA

[4], and responsive neurostimulators [5]. Active, electrically powered implants pose significant safety risks for the human body, including current leakage and thermal injury. Excessive heat dissipation from an active implant can lead to irreversible damage of cells and tissues, including necrosis [6]. Therefore, the Food and Drug Administration (FDA) imposes stringent limitations on the thermal impact of active implants.

Many of these systems employ an enclosure made out of titanium and other biocompatible materials, which is subcutaneously implanted in the pre-pectoral area. These chest wall units (CWUs) typically house a battery, an electrical stimulator, as well as control and communication modules. Inspired by this common design, our group has been developing a fully-implantable electrocorticogram (ECoG)-based bi-directional brain—computer interface (BD-BCI) system (see Fig. 1). This system is intended to restore walking and leg sensation in people with paraplegia due to spinal cord injury (SCI). Specifically, we envision this system to decode leg motor intentions, actuate the leg prosthesis, sense the movement, and deliver artificial leg sensation by cortical electrostimulation. Our group has been working on such a system for several years, developing custom analog



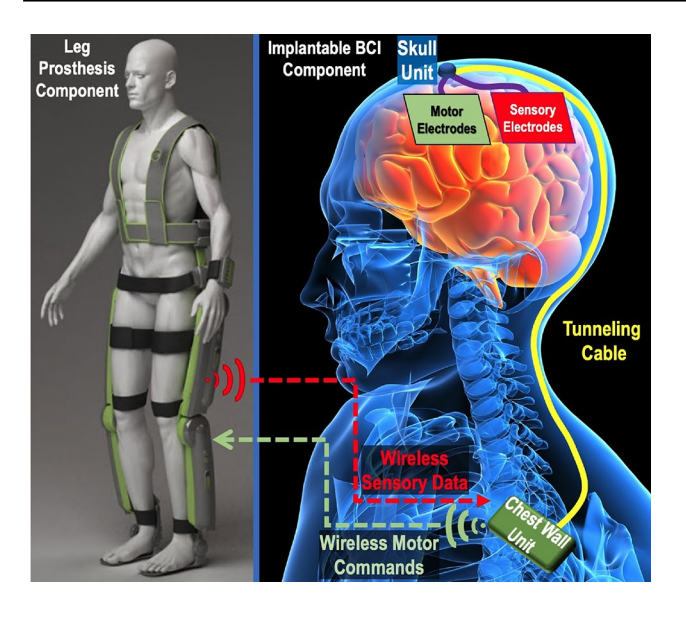
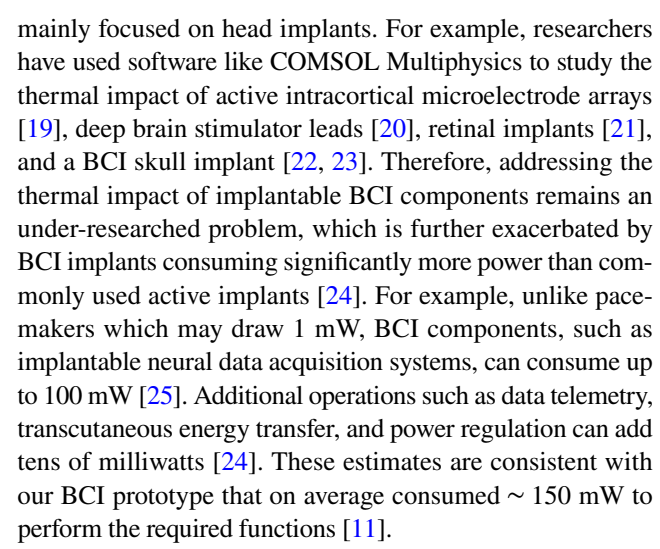


Fig. 1 The envisioned fully-implantable ECoG-based BCI system for restoration of walking and leg sensation after SCI. (Left) Leg prosthesis component consisting of an exoskeleton for walking. (Right) Implantable BCI components and connections. The motor electrodes on the leg cortex record leg movement intentions. These signals are routed to a skull unit (SU), where they are amplified, serialized, and digitized. A subcutaneously implanted tunneling cable (similar to current DBS systems) sends them to the CWU, where they are analyzed and decoded. The CWU wirelessly transmits commands to the exoskeleton. The CWU also receives sensor data from the exoskeleton and translates it into stimulation patterns. These are routed through the tunneling cable to the SU and delivered to the leg sensory cortex via sensory electrodes to elicit artificial leg sensation. The implants' dimensions and positions are for illustration purposes.

ultra-low-power (ULP) front ends for recording [7–9], a low-power transceiver for wireless communication [10], and a benchtop prototype of the overall system [11, 12].

The CWU processes motor and sensory data, controls all auxiliary BCI components, and communicates wirelessly with an end effector; therefore, it is the most "power-hungry" component of the system. Thus, we must evaluate its thermal impact on the surrounding tissues to ensure thermal safety. To this end, we propose to use computational models to estimate CWU's maximum power budget that guarantees its thermally safe operation. While previous studies have used computational models to analyze the thermal impact of active implants, to the best of our knowledge, there are no studies on the long-term thermal impact of CWU-like implantable devices. Researchers have used numerical models to simulate the thermal behavior of pacemakers [13] and deep brain stimulators [14, 15] under transient overheating conditions, like MRI scanning. Others have used simulations to analyze the thermal effects of specific operations, like biotelemetry for head and chest implants [16], deep neural implants [17], and cortical implants [18]. On the other hand, the studies that have modeled the long-term thermal effects of active devices have



Motivated by this knowledge gap, we sought to evaluate the thermal impact of a subcutaneously implanted CWU on adjacent pectoral area tissues. To this end, we used the Finite Element Method (FEM) implemented in COMSOL Multiphysics (COMSOL Inc., Stockholm, Sweden) to simulate the temperature of nearby tissues in response to various CWU power consumption levels. We refer to this model as the bio-heat model. Furthermore, we performed a sensitivity analysis to assess the robustness of this bio-heat model against the natural variations of the physiological and environmental parameters. This analysis also yielded the prediction of a thermally safe CWU power budget range. Our ultimate goal is to verify these predictions in vivo and will be pursued in our future studies. In the interim, to validate our modeling approach we performed benchtop experiments. Specifically, we built a thermal prototype of CWU and measured its temperature under different power consumption levels. We then designed a COMSOL model of the thermal prototype (benchtop model), simulated its thermal behavior, and compared these results to those obtained experimentally.

Materials & Methods

In this section, we first present the details of our computational bio-heat model, including its geometry and mathematical description. We also present a sensitivity analysis of the bio-heat model and a benchtop validation of our computational approach.

Bio-heat Model

Geometry

The simulated geometry represents a rectangular region (150 \times 150 \times 72 mm) of the thoracic cavity (see Fig. 2). The skin was assumed to be in direct contact with the air. We further assumed that the CWU is placed below the clavicle



Table 1 The average thickness of the relevant tissue layers

Tissue	Thickness, l (mm)	References	
Skin	2.5	[28]	
Fat	4.7	[29]	
Muscle	8.4	[30]	
Ribs	6.0	[31]	

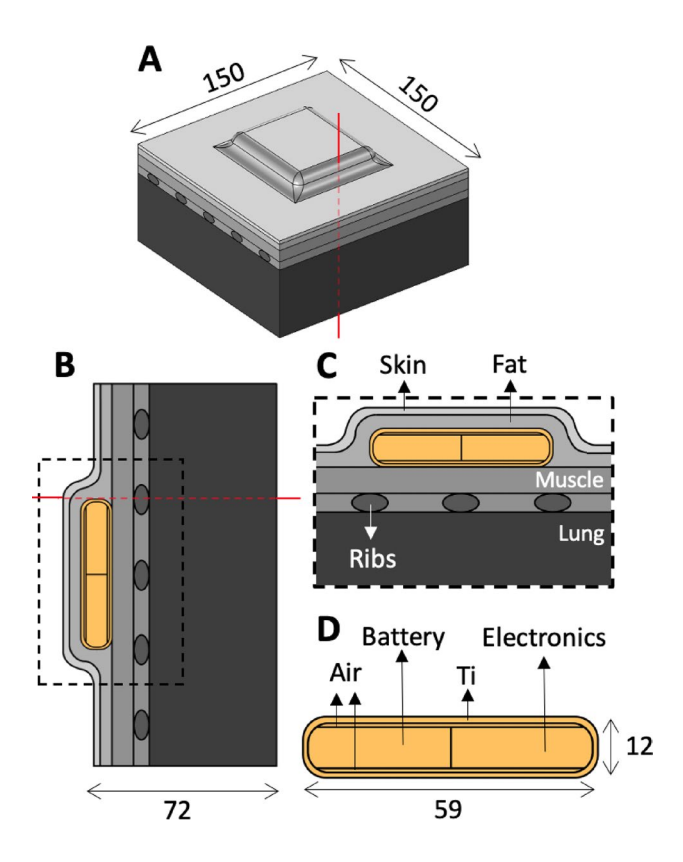


Fig. 2 Geometric model of the thoracic area and CWU from different views, dimensions in mm. A 3D view. The red line indicates the axis where the thermal impact due to the CWU is highest, see Sect. "Bio-heat Model" for details. B Central cross-section of the volume in (A). C A zoomed-in view of the inset in (B). D Different layers of the CWU.

(pre-pectoral implantation), under the skin and fat tissues, but above the pectoral muscle, similar to implantable pulse generators (IPGs) for pacemakers [26] and DBS [27]. This model also included the ribs, surrounded by intercostal muscle, and lung tissue. Each tissue's thickness was taken from literature with specific values listed in Table 1.

The CWU was modeled as a rectangular prism $(59 \times 50 \times 12 \text{ mm})$ made out of a 1-mm-thick titanium (Ti) shell (Fig. 2). Note that these dimensions are well within the range of common IPG enclosures [27]. We envision the CWU to contain a battery and an electronics layer consisting of a printed circuit board (PCB) with the necessary electronic components. We modeled the battery and electronics as

adjacent 8-mm-thick blocks of equal size, surrounded by 1-mm air gap on top and bottom. This arrangement of the battery and electronic components as well as their overall volumes were inspired by the design of commonly used IPGs [27, 32].

Bio-heat equation

Heat transfer through biological tissues is typically described by Penne's bio-heat equation [33]:

$$\rho C \frac{\partial T}{\partial t} = k \nabla^2 T - \rho_b C_b \omega (T - T_b) + Q_m + Q_{\text{ext}}, \tag{1}$$

where ρ (kg/m³) and C (J/(kg K)) are the tissue's mass density and specific heat capacity, respectively, and T (K) is the temperature at a position (x, y, z) and time t. The first term on the right-hand side is the heat conduction, where k(W/(m K)) is the tissue's thermal conductivity. The second term models the effect of blood perfusion, where ω ((ml/s)/ ml) is the volumetric flow rate of the perfusing blood per unit volume and the subscript, b, refers to arterial blood. Finally, the term $Q_{\rm m}$ (W/m³) is the metabolic heat produced by the tissue, and $Q_{\rm ext}$ (W/m³) is the heat produced by external sources (e.g., the CWU). Note that $Q_{\rm ext} = 0$ for all layers except for the electronics layer. It is defined as $Q_{\text{ext}} = P_{\text{CWU}}/V_{\text{elec}}$, where P_{CWU} (W) is the CWU's power consumption and V_{elec} (m³) is the volume of the electronics layer. The software applied the partial differential equation (PDE) given by Eq. (1) to all tissue layers and CWU components, setting to 0 those terms that do not apply and enforcing temperature continuity at the layer interfaces. To study the long-term thermal effects of the CWU, we solved the steady-state solution of Eq. (1).

The thermal parameters for each tissue layer are given in Table 2. The tissue's thermal conductivity can vary by as much as 50%; therefore, we took the average values as reported in [34]. Similarly, we computed the tissues' metabolic heat as the average of the values found in [35] and [36]. Since the tissues' blood perfusion significantly depends on physical activity, we used the values corresponding to light exercise or slow walking (1 mph, 80 bpm). Specifically, the fat and ribs' blood perfusion values were estimated from [37] and [38], respectively. For the muscle's blood perfusion, we first estimated the oxygen consumption corresponding to light exercise (0.4 l/min) [39] and then used this information to estimate the blood perfusion from [40], which provides a link between oxygen consumption and blood perfusion. Likewise, for the lungs' blood perfusion, we first estimated the mean pulmonary artery pressure associated with light exercise (17 mmHg) [41] and then used this value to estimate blood perfusion from [42], which gives the relationship between blood perfusion and pulmonary artery pressure. Finally,



Table 2 The average values of tissues' thermal parameters: thermal conductivity, k, metabolic heat, $Q_{\rm m}$, and blood perfusion, $\rho_b C_b \omega$

	k W/(m K)	$Q_{\rm m}$ W/m ³	$\rho_{\rm b}C_{\rm b}\omega{\rm W/(m^3~K)}$	References
Skin	0.36	1004	5192	[34, 35, 43]
Fat	0.24	180	1504	[34, 36, 37]
Muscle	0.50	661	3580	[34, 36, 40]
Ribs	0.43	0	1232	[34, 35, 38]
Lungs	0.44	370	222589	[34, 35, 42]

we estimated that during light exercise the skin's blood perfusion increases 9% with respect to resting state [43], and we computed the blood perfusion at rest as the average of the values found in [43–49].

The thermal conductivities of the titanium shell and air were 19 W/(m K) [50] and 0.03 W/(m K) [51], respectively. Due to its internal multi-layer structure, the battery has a highly anisotropic thermal conductivity, with $k_{xy} = 15$ and $k_z = 1$ (W/(m K)) [52]. For the electronics layer, we assumed that its thermal properties are similar to those of the PCB. Similar to the battery, the PCB's thermal conductivity is also anisotropic and depends on the number of layers. For a six-layer PCB, as used in our preliminary benchtop CWU prototype [11], we estimated the thermal conductivity as $k_{xy} = 28.15$ and $k_z = 0.31$ (W/(m K)), based on formulas provided in [53].

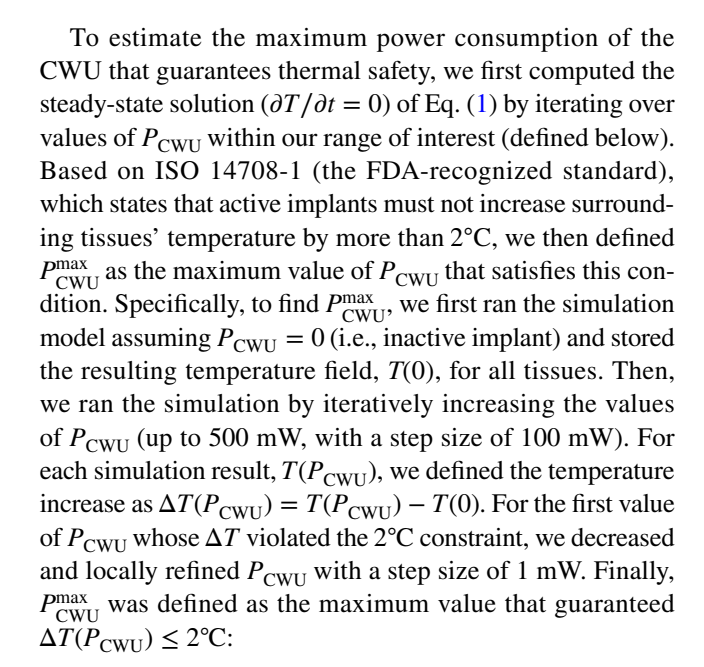
We applied the following boundary conditions to the boundary value problem (1). Consistent with [19] and [21], we assumed that heat transfer occurred through free convection at the skin-air interface:

$$\mathbf{n} \cdot (k\nabla T) = h(T_{\text{ext}} - T),\tag{2}$$

where **n** is the outward normal vector, h (W/m²K) is the convection heat transfer coefficient ,and $T_{\rm ext}$ (K) is the room temperature. For this model, we used h = 5 W/(m³K), which corresponds to free airflow in the environment [54] and $T_{\rm ext} = 20^{\circ}$ C. Consistent with other studies, we omitted the effect of radiation from the skin surface to the outside air [19]. For the innermost boundary, we assumed the temperature to be equal to the body core temperature [19, 20], with $T = 37^{\circ}$ C [55]. Finally, we assumed that there was no heat transfer across the lateral boundary:

$$\mathbf{n} \cdot (k \nabla T) = 0. \tag{3}$$

This assumption is justified given the relatively large distance between the lateral boundary and the CWU heat source. Therefore, the temperature gradients at the lateral boundary are negligible. We will refer to the parameters described here and Sect. "Geometry" as the nominal parameters.



$$P_{\mathrm{CWU}}^{\max} = \underset{P_{\mathrm{CWU}} \in [0,500]}{\arg \max} \Delta T(P_{\mathrm{CWU}}) : \Delta T(P_{\mathrm{CWU}}) \le 2^{\circ} \mathrm{C}. \tag{4}$$

Sensitivity Analysis

We performed a sensitivity analysis to ensure the robustness of our prediction against the natural variations of physiological and environmental parameters. To this end, the nominal parameters introduced in the previous section were perturbed in both directions based on their physiological and environmental variance. Specifically, we considered the effect of perturbing the following 21 parameters: all those in Tables 1 and 2, $T_{\rm ext}$, $T_{\rm core}$, and h. We omitted perturbing the parameters pertaining to the geometry and materials of CWU, given that the CWU's design is fixed.

Table 3 lists these parameters with their nominal and perturbed values. The upper and lower values for the tissues' thickness, l, were taken from [28–31]. For the thermal conductivity, k, the negative and positive perturbation values were estimated from [34]. For the metabolic heat, $Q_{\rm m}$, the perturbation bounds for the fat and muscle tissues were taken from [36]. Since physiological ranges for the skin and lungs were not available, we estimated their variance at $\pm 10\%$ (the average perturbation from fat and muscle). On the other hand, the lower bounds of blood perfusion were estimated from values at rest, while the upper bounds were estimated from values at double the nominal walking speed (2 mph, 90 bpm). The skin's blood perfusion at rest was estimated as the average of the values from [43–49]. Similarly, the fat's blood perfusion value at rest was estimated from [37, 46–49], and the muscle's blood perfusion at rest was estimated from [44-49, 56]. The ribs' resting blood perfusion was taken from [49], and the lungs' blood perfusion



Table 3 The nominal parameters, θ_i^o and their negatively and positively perturbed values, θ_i^* and θ_i^+ , respectively

$\overline{\theta_i}$	θ_i^0	$ heta_i^{\scriptscriptstyle -}$	θ_i^+
$\theta_1 = l^{\text{skin}}$	2.50	2.24	2.88
$\theta_2 = l^{\text{fat}}$	4.70	1.98	7.90
$\theta_3 = l^{\text{muscle}}$	8.40	7.78	9.02
$\theta_4 = l^{\mathrm{rib}}$	6.00	4.00	8.00
$\theta_5 = \omega^{\text{skin}}$	5192.00	4751.00	6413.00
$\theta_6 = \omega^{\mathrm{fat}}$	1504.00	1331.00	1909.00
$\theta_7 = \omega^{\text{muscle}}$	3580.00	1896.00	5897.00
$\theta_8 = \omega^{\rm rib}$	1232.00	847.00	1617.00
$\theta_9 = \omega^{\text{lung}}$	222589.00	133173.00	317713.00
$\theta_{10} = Q_{\mathrm{m}}^{\mathrm{skin}}$	1004.00	904.00	1104.00
$\theta_{11} = Q_{\rm m}^{\rm fat}$	198.00	169.00	214.00
$\theta_{12} = Q_{\rm m}^{\rm muscle}$	694.00	640.00	759.00
$\theta_{13} = Q_{\rm m}^{\rm lung}$	370.00	333.00	407.00
$\theta_{14} = k^{\text{skin}}$	0.36	0.25	0.47
$\theta_{15} = k^{\text{fat}}$	0.24	0.22	0.26
$\theta_{16} = k^{\text{muscle}}$	0.50	0.49	0.51
$\theta_{17} = k^{\text{rib}}$	0.43	0.34	0.52
$\theta_{18} = k^{\text{lung}}$	0.44	0.42	0.46
$\theta_{19} = T_{\rm b}$	37.00	36.50	39.50
$\theta_{20} = h$	5.00	2.50	25.00
$\theta_{21} = T_{\text{ext}}$	20.00	5.00	35.00

value at rest was taken from [42]. The upper bound values for blood perfusion for the skin, fat, muscle, ribs, and lungs were estimated from [37, 38, 40, 42, 43], respectively. Additionally, the range for the heat transfer coefficient, h, was taken from [54]. Finally, we approximated the natural variations of the temperatures $T_{\rm b}$ and $T_{\rm ext}$.

Our sensitivity analysis was based on calculating the sensitivity coefficient, S_i , defined as the relative change of $\Delta T(P_{\text{CWU}})$ over the relative change of the parameter θ_i [57]:

$$\begin{split} S_i &= \frac{\left(\Delta T(P_{\mathrm{CWU}}^{\mathrm{max}}, \boldsymbol{\Theta}_i^*) - \Delta T(P_{\mathrm{CWU}}^{\mathrm{max}}, \boldsymbol{\Theta}^0)\right) / \Delta T(P_{\mathrm{CWU}}^{\mathrm{max}}, \boldsymbol{\Theta}^0)}{\left(\boldsymbol{\theta}_i^* - \boldsymbol{\theta}_i^0\right) / \boldsymbol{\theta}_i^0}, \\ i &= 1, 2, \cdots, 21 \end{split}$$

In other words, S_i quantifies the impact that the variation of the parameter θ_i has on the tissue's temperature increase in our bio-heat model. In Eq. (5), $\Delta T(P_{\text{CWU}}^{\text{max}}, \Theta^0)$ is the maximum temperature increase across all tissues corresponding to $P_{\text{CWU}}^{\text{max}}$ and Θ^0 , where $\Theta^0 = [\theta_1^0, \theta_2^0, \cdots, \theta_{21}^0]$ is the vector of perturbed nominal parameters as shown in Table 3. Likewise, $\Delta T(P_{\text{CWU}}^{\text{max}}, \Theta_i^*)$ is the maximum temperature increase across all tissues corresponding to $P_{\text{CWU}}^{\text{max}}$ and Θ_i^* , where $\Theta_i^* = [\theta_1^0, \cdots, \theta_i^*, \cdots, \theta_{21}^0]$ and θ_i^* is the perturbed value of the ith parameter. To quantify sensitivity in both directions,

for each parameter θ_i , we calculated S_i^+ , corresponding to $\theta_i^* = \theta_i^+$ (positive perturbation), and S_i^- , corresponding to $\theta_i^* = \theta_i^-$ (negative perturbation), as shown in Table 3.

Based on these sensitivity coefficients, we defined critical parameters as those whose perturbations considerably affected the bio-heat model, i.e., $|S_i| > 10^{-4}$. In other words, the parameters whose relative change of 1% resulted in a relative change of $\Delta T < 10^{-4}\%$ were considered non-critical. Since Eq. (5) considers the perturbation of a single parameter at a time, we also sought to investigate the effects of perturbing multiple parameters simultaneously. This is necessary to account for the interactions between parameters and to get a more realistic idea of the potential variations that the bio-heat model could experience. For this reason, we re-estimated P_{CWI}^{max} while simultaneously perturbing all the critical parameters. Specifically, we ran simulations for the worst-case scenario (WCS) and best-case scenario (BCS). In the WCS, we perturbed the critical parameters in the direction that would lead to an increase in ΔT , which, in turn, would reduce the CWU's power budget. On the other hand, for the BCS, we perturbed the critical parameters in the direction that would lead to a decrease in ΔT , which would result in a higher power budget. In both scenarios the non-critical parameters were held at their nominal values. We will refer to the re-estimated power budgets for each scenario as $P_{\text{CWU}}^{\text{WCS}}$ and $P_{\text{CWU}}^{\text{BCS}}$.

Benchtop Validation

We used benchtop open-air experiments to validate our modeling approach. Ultimately, our power budget predictions will be confirmed using in vivo testing and will be pursued in our future studies (see Sect. "Discussion"). An alternative approach would have been to perform in vitro experiments using phantom tissues. For example, we made skin, fat, and muscle phantom tissues to test the wireless communication capabilities of our CWU prototype [10]. Unlike electrical conductivity and permittivity, which we could easily manipulate in phantom tissues, metabolic heat production and blood perfusion effects cannot be easily replicated [58]. Furthermore, our sensitivity analysis shows that blood perfusion is among the most critical parameters of the bio-heat model. Thus, our bio-heat model could not be accurately reproduced in vitro, and as an alternative, we chose to validate our modeling approach using benchtop open-air experiments. To this end, we built a thermal replica of the CWU with a Ti enclosure whose dimensions and power consumption levels match those of the bio-heat model. We then measured the surface temperature of this thermal prototype in an open-air experiment and compared these experimental results to those obtained via simulations.



Specifically, we fabricated the thermal prototype as a rectangular-shaped prism (59 \times 50 \times 12 mm), assembled from two clamshell Ti alloy (ASTM B265 Grade 2) parts, which were laser welded in a hermetic fashion. This alloy is a commonly used material for medical implants due to its biocompatibility [59]. The Ti case (1-mm-thick shell) encloses a PCB with resistors to mimic the CWU's electronic layer and a battery connected to external switches (see Fig. 3A and B). With these switches, the prototype could be powered and set to operate at one of four power consumption levels (300, 400, 500, and 600 mW). The prototype also had a connector to enable the battery to be charged externally. Note that the thermal prototype dimensions, enclosure material, wall thickness, and power consumption levels closely match those of the bio-heat model described in Sect. "Bioheat Model." With the exception of the connector cables, the arrangement of the battery and resistors also mimics the arrangement of the battery and electronic layer within the CWU.

For each power consumption level, we conducted an open-air experiment, as described below. We placed the thermal prototype on a laminate wood benchtop, turned the prototype on with a certain power consumption configuration, and waited for one hour for heat to reach a quasi-steady state. Next, we measured the prototype's top surface temperature using both a thermocouple, $T_{\rm p,t}$ and a thermal camera (FLIR C2, Teledyne FLIR, Wilsonville, OR), $T_{\rm p,c}(x,y)$. To minimize reflection and accommodate more accurate temperature measurements with the thermal camera, we painted the top surface of the prototype black. We also took

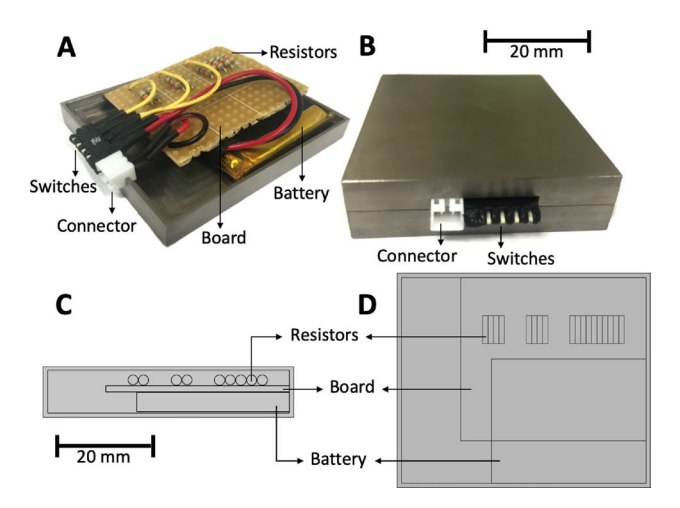


Fig. 3 Different views of our custom-designed CWU thermal prototype and its COMSOL model. **A** View of the prototype's interior prior to laser-welding the two clamshells. Different switch positions engage different combinations of resistors for the prototype to operate at different powers. **B** A front view of the laser-welded prototype. **C** Cross-section of the prototype's COMSOL model (lateral view). **D** Cross-section of the prototype's model (top view).

periodic measurements of the room temperature, $T_{\rm ext}$, the battery's voltage, $V_{\rm b}$, and its current, $I_{\rm b}$, since these variables changed over time, thus affecting the prototype's surface temperature. Specifically, the room-temperature measurements were taken with a thermocouple in close proximity to the air surrounding the prototype and repeated every 10 min for about an hour. Moreover, we measured the battery's voltage and current every 10 min from the moment the prototype was powered until the end of the experiment. These measurements were taken using a digital multimeter (Tenma 72-8400, Tenma Test Equipment, Springboro, OH). Note that as the battery discharges over time, $V_{\rm b}$ decreases, which, in turn, lowers the prototype's instantaneous power consumption.

We then created a COMSOL model of the CWU thermal prototype in an open-air environment, which we refer to as the benchtop model. Its dimensions precisely matched those of the thermal prototype, including the 1-mm Ti shell, battery $(36 \times 29 \times 4.7 \text{ mm})$, resistors (2.5 mm diameter, 6.5 mm length), and board $(43 \times 38 \times 1.6 \text{ mm})$, as shown in Fig. 3C and D. The prototype was modeled sitting on top of a rectangular laminate wood benchtop $(600 \times 600 \times 30 \text{ mm})$.

We modeled heat transfer using the same approach as in the bio-heat model (see Sect. "Bio-heat equation"). Given that metabolic heat and blood perfusion do not apply to the benchtop model, we set $Q_{\rm m}$ and ω from Eq. (1) to 0. Analogous to the bio-heat model, the software applied this PDE to each component of the benchtop model and computed its steady-state solution. To do so, we first chose the parameters of the benchtop model as follows. We set the thermal conductivity, k, of Ti (ASTM B265 Grade 2) and the benchtop's laminated wood to be 21.8 W/(m K) [60] and 0.12 W/ (m K) [61], respectively. We also set the thermal conductivity of the resistors and board to be 1.88 W/(m K) [62] and 0.29 W/(m K) [63], respectively. Additionally, we kept the thermal conductivity of the battery and air the same as in the bio-heat model (see Sect. "Bio-heat equation"). Finally, we defined the heat source as $Q_{\text{ext}} = P_{\text{b}}/V_{\text{R}}$, where P_{b} is the battery's power usage and V_R is the overall volume of the selected resistors, as determined by the combination of switches. The battery's power was estimated as $P_b = V_b \times I_b$, where $V_{\rm h}$ and $I_{\rm h}$ were measured throughout the benchtop experiments, as described above.

For this boundary problem, we enforced temperature continuity at the benchtop-prototype interface and all other internal interfaces. We also assumed that the heat transfer occurred through free convection on all external boundaries, similar to the skin-air boundary of the bio-heat model, Eq. (2). In this equation, we estimated the room temperature, $T_{\rm ext}$, as the time average of the temperature measurements taken throughout the benchtop experiment. Another critical parameter of this equation is the heat transfer coefficient, h, which is sensitive to local air flow and temperature, and



can vary greatly across environments [54]. Therefore, we estimated h experimentally using Newton's law of cooling. Specifically, a $306 \times 52 \times 10$ -mm Ti (ASTM B265 Grade 2) bar was placed in the oven and heated to at least 40° C above the room temperature. Then, the bar was removed from the oven and placed on the same benchtop as the thermal prototype to let it cool. The bar's temperature was recorded every 30 s for about an hour. These measurements were then used to fit a linear regression to the logarithmic form of the cooling equation:

$$\ln \frac{\Delta T(t)}{\Delta T(0)} = -\frac{hA}{mc}t,$$
(6)

where $\Delta T(t) = T_{\rm bar}(t) - T_{\rm r}$, $T_{\rm bar}(t)$ is the time dependent-temperature of the bar, and $T_{\rm r}$ is the room air temperature, respectively. The parameters A, m, and c are the area (m²), mass (kg), and heat capacity (J/(kg K)) of the Ti bar, respectively.

For each of the four experiments, we simulated the COM-SOL benchtop model twice and compared these results to the experimental measurements. This was necessary to reconcile a constant power consumption assumed by the steadystate solution of Eq. (1) and a decreasing power consumption observed experimentally due to battery draining over the course of each experiment. Specifically, we simulated the model while assuming two extreme power consumptions, $P_{\rm b}^{\rm max}$ and $P_{\rm b}^{\rm min}$, which were derived from the battery voltage and current measurements taken at the beginning and end of each benchtop experiment. For each case, we computed the average temperature of the modeled prototype's top surface, $T_{\rm m}(P_{\rm b}^{\rm max})$ and $T_{\rm m}(P_{\rm b}^{\rm min})$, respectively. These values were then compared to the experimentally derived temperature $T_{\rm p}$, where $T_{\rm p}$ is the average of the thermal image measurements, $T_{\rm p,c}$ (averaged over space), and the thermocouple measurements, $T_{p,t}$. The value T_p was calculated every 10 min and compared to the simulated range $[T_m(P_h^{min})]$ and $T_m(P_h^{max})$.

Results

Bio-heat Model

We simulated the bio-heat model in Eq. (1) using the FEM in COMSOL. To determine the appropriate mesh size, we used an adaptive physics-controlled mesh algorithm. Specifically, we solved Eq. (1) using the following predefined COMSOL mesh sizes: coarser, coarse, normal, fine, finer, and extra fine. The difference in the resulting temperature going from coarser to extra fine mesh size kept decreasing, with the difference between the finer and extra fine mesh size being < 0.001° C. This suggested that the simulation had converged with respect to the mesh size [19]. Therefore,

we chose the *finer* mesh size in our bio-heat model to balance accuracy and computational cost. We ran the simulations using the geometric parameters shown in Table 1 and Sect. "Geometry," and the thermal parameters from Table 2 and Sect. "Bio-heat equation."

We found $P_{\text{CWU}}^{\text{max}}$ by the iterative procedure described in Sect. "Bio-heat equation." To simplify the interpretation of volumetric temperature data, we focused on the worstcase scenario line segment (marked by the red-dashed line in Fig. 2A), where the thermal impact due to the CWU, judged by $\Delta T(P_{CWII})$, is highest. Figure 4 shows the simulated $\Delta T(P_{\text{CWII}})$ along this segment for different values of P_{CWU} within our range of interest. For all power consumption levels, we observed the highest temperature increase in the fat layer, followed by the muscle, skin, ribs, and lungs. We also observed that ΔT peaked at the same depth, $d^* \approx 12.2$ mm, for all power levels. This depth corresponds to the point where the worst-case scenario line is tangential to the implant. This figure also shows that $\Delta T(500)$ violated the 2°C threshold in the fat tissue layer. Therefore, we iterated the value of P_{CWII} below 500 mW with a precision of 1 mW, and we found the maximum power consumption to be $P_{\text{CWU}}^{\text{max}} = 458 \text{ mW}$. Figure 4 confirms that $\Delta T(458) \leq 2^{\circ}\text{C}$ for all tissue layers.

Figure 5 shows the 2D distribution of ΔT corresponding to the maximum power consumption, $P_{\text{CWU}}^{\text{max}} = 458 \,\text{mW}$, over the central cross-section. Consistent with Fig. 4, the highest tissue temperature increase occurred in the fat tissue. Note that ΔT exceeded the 2°C thermal safety threshold in the

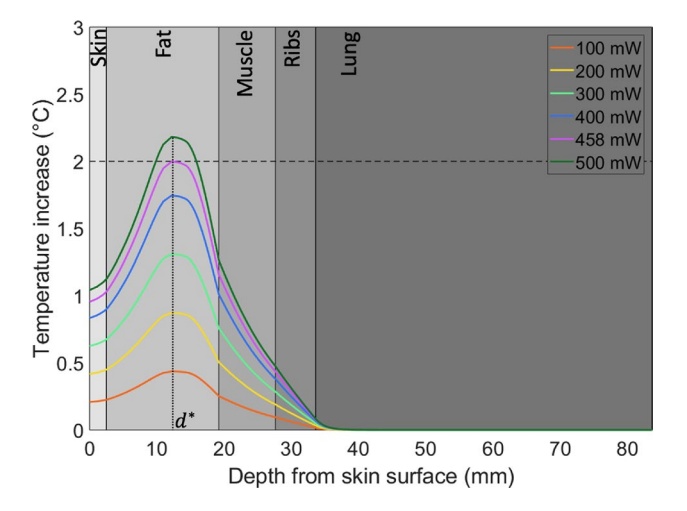


Fig. 4 Temperature increase, $\Delta T(P_{\rm CWU})$, for different values of $P_{\rm CWU}$, calculated along the axis of the CWU with the tissues' highest ΔT . This region undergoes the highest thermal impact within the overall geometry. The solid vertical lines mark the boundaries of each layer, which are colored in different shades of gray and labeled at the top. The dashed horizontal line marks the 2° C thermal safety threshold. The dotted vertical line marks the depth, d^* , at which ΔT is highest for all power levels.



interior of CWU (parts of the electronics layer and Ti shell). However, only the biological tissues are subjected to the thermal safety threshold.

Sensitivity Analysis

To quantify the robustness of the bio-heat model with respect to the nominal parameter values, we computed the sensitivity coefficient, S_i , for all the parameters, θ_i ($i=1,2,\cdots,21$). Table 4 shows the values of S_i for the positive and negative perturbations as shown in Table 3. Based on the criteria $|S_i| > 10^{-4}$, the simulation results were sensitive to 15 critical parameters. The perturbations of the remaining 6 noncritical parameters did not significantly alter the simulation results.

Finally, we modeled the combined effect of all the critical parameters. We perturbed the 15 critical parameters simultaneously (while keeping the nominal values of the non-critical parameters) to simulate a worst and best-case scenario. We then re-estimated the maximum power consumption for each case, namely $P_{\rm CWU}^{\rm WCS}$ and $P_{\rm CWU}^{\rm BCS}$, and found the power budget range to be between 378 mW and 538 mW.

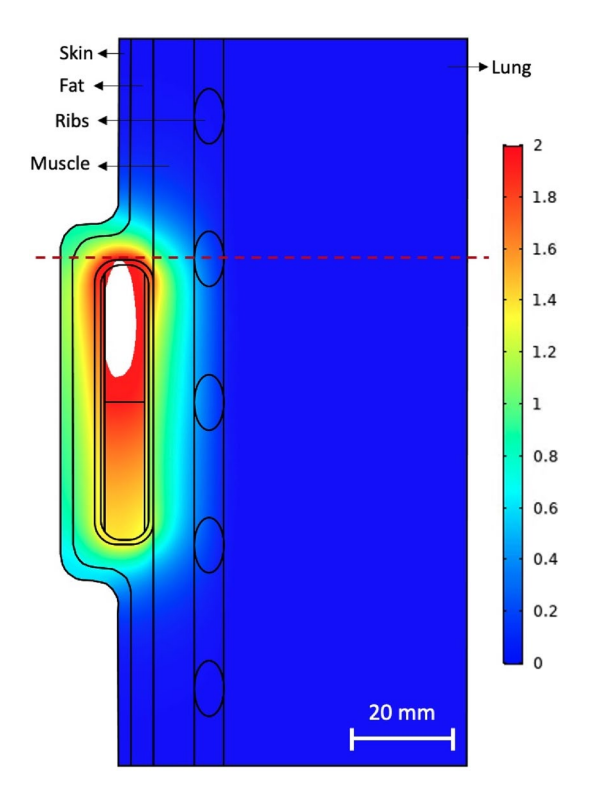


Fig. 5 ΔT (458) in °C over the central 2D cross-section from Fig. 2B. Areas where $\Delta T > 2$ °C were not assigned a color to visually preserve the temperature resolution. The red-dashed line indicates the axis with the tissues' highest ΔT .



Table 4 The sensitivity coefficients, S_i^- and S_i^+ , for the respective perturbation of each parameter, as indicated in Table 3. The critical parameters are highlighted in gray

$\overline{ heta_i}$	S_i^-	S_i^+
$\theta_1 = l^{\text{skin}}$	-9.43·10 ⁻²	-8.28·10 ⁻²
$\theta_2 = l^{\mathrm{fat}}$	$-3.64 \cdot 10^{-2}$	$-1.39 \cdot 10^{-2}$
$\theta_3 = l^{\text{muscle}}$	$4.42 \cdot 10^{-2}$	$3.88 \cdot 10^{-2}$
$\theta_4 = l^{\mathrm{rib}}$	$4.27 \cdot 10^{-2}$	$2.99 \cdot 10^{-2}$
$\theta_5 = \omega^{\text{skin}}$	$-8.21 \cdot 10^{-2}$	$-7.34 \cdot 10^{-2}$
$\theta_6 = \omega^{\text{fat}}$	$-8.31 \cdot 10^{-2}$	$-7.89 \cdot 10^{-2}$
$\theta_7 = \omega^{\text{muscle}}$	$-1.01 \cdot 10^{-1}$	$-7.55 \cdot 10^{-2}$
$\theta_8 = \omega^{\text{rib}}$	$-7.34 \cdot 10^{-4}$	$-7.25 \cdot 10^{-4}$
$\theta_9 = \omega^{\text{lung}}$	$-6.49 \cdot 10^{-3}$	$-3.60 \cdot 10^{-3}$
$\theta_{10} = Q_{\mathrm{m}}^{\mathrm{skin}}$	$2.34 \cdot 10^{-8}$	$2.34 \cdot 10^{-8}$
$\theta_{11} = Q_{ m m}^{ m fat}$	$1.19 \cdot 10^{-8}$	$1.19 \cdot 10^{-8}$
$\theta_{12} = Q_{\rm m}^{\rm muscle}$	$7.05 \cdot 10^{-10}$	$7.07 \cdot 10^{-10}$
$\theta_{13} = Q_{\rm m}^{\rm lung}$	$-4.21 \cdot 10^{-10}$	$-4.15 \cdot 10^{-12}$
$\theta_{14} = k^{\text{skin}}$	$-3.45 \cdot 10^{-2}$	$-1.20 \cdot 10^{-2}$
$\theta_{15} = k^{\text{fat}}$	$-2.48 \cdot 10^{-1}$	$-2.22 \cdot 10^{-1}$
$\theta_{16} = k^{\text{muscle}}$	$-2.32 \cdot 10^{-1}$	$-2.27 \cdot 10^{-1}$
$\theta_{17} = k^{\text{rib}}$	$-1.53 \cdot 10^{-2}$	$-1.24 \cdot 10^{-2}$
$\theta_{18} = k^{\text{lung}}$	$-4.77 \cdot 10^{-3}$	$-4.48 \cdot 10^{-3}$
$\theta_{19} = T_{\rm b}$	$-1.09 \cdot 10^{-6}$	$-1.42 \cdot 10^{-6}$
$\theta_{20} = h$	$-2.29 \cdot 10^{-2}$	$-1.45 \cdot 10^{-2}$
$\theta_{21} = T_{\text{ext}}$	$1.00 \cdot 10^{-5}$	$8.78 \cdot 10^{-5}$

Benchtop Validation

The benchtop experiments were performed in a dedicated room with minimal disturbance from external factors. As explained in Sect. "Benchtop Validation," we placed the CWU thermal prototype on the benchtop, turned the power on, and waited for one hour before taking temperature measurements from the device's surface. We also periodically measured the room temperature, as well as the battery's voltage and current throughout the experiment. We repeated the experiment for the nominal power consumption levels of 300, 400, 500, and 600 mW. Figure 6A shows a representative example of the prototype's quasi-steady-state surface temperature for the 500-mW set-up.

We then simulated these experiments in COM-SOL, using our benchtop computational model (see Sect. "Benchtop Validation"). Consistent with the bioheat model, we used the predefined *finer* mesh setting for these simulations. The model used the parameters specified in Sect. "Benchtop Validation," except for the heat transfer coefficient, h. As explained earlier, this parameter critically depends on the environment and, therefore, had to be determined experimentally in the same dedicated room as above. To this end, we used the Ti bar temperature

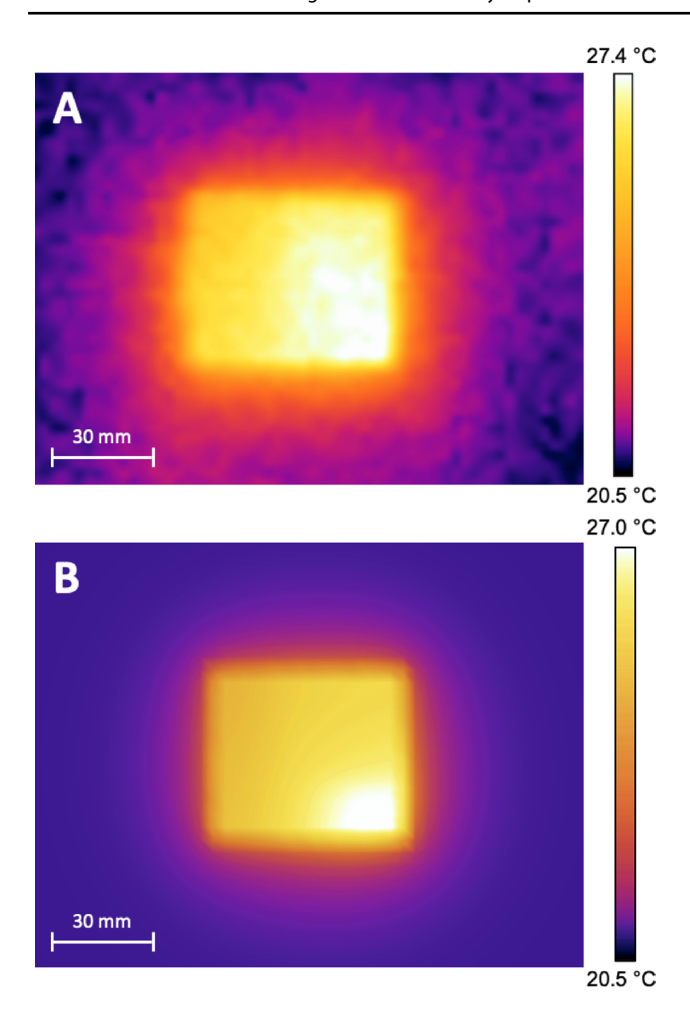


Fig. 6 2D temperature maps of the CWU thermal prototype and its benchtop COMSOL model for the 500-mW configuration. The bright spot in the lower right corner overlaps with the position of the resistors. **A** Thermal camera image of the prototype placed on the benchtop. **B** An equivalent map produced by the benchtop computational model with $T_{\rm ext} = 22.9^{\circ}{\rm C}$.

decay experiment to fit a linear regression based on Eq. (6) with $A = 0.016 \text{ m}^2$, m = 0.718 kg, and c = 523 J/(kg K) [64]. This resulted in a heat transfer coefficient estimate $h = 13 \text{ W/(m}^3\text{K)}$. Figure 7 shows the temperature decay measured experimentally, as well as the prediction based on this value of h. Note that the goodness-of-fit measure, $R^2 = 0.995$, suggests a high concordance between experimental data and model prediction. Once h was found, we simulated the benchtop model at the four nominal power consumption levels. Figure 6B shows an example of the simulated prototype's surface temperature distribution for the 500-mW power consumption.

From experimental data, we calculated the thermal prototype's average surface temperature, $T_{\rm p}$, every 10 min, and compared these values to the simulated range $[T_{\rm m}(P_{\rm b}^{\rm min}), T_{\rm m}(P_{\rm b}^{\rm max})]$ (see Sect. "Benchtop Validation"). Figure 8 shows the results at the four nominal power

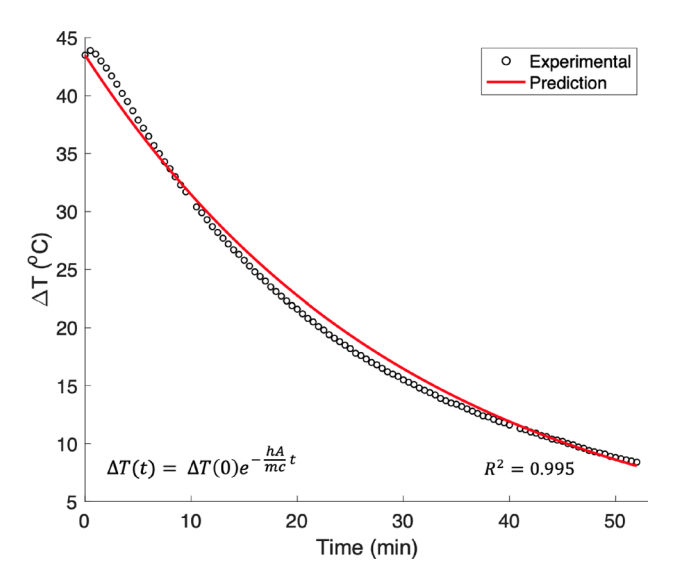


Fig. 7 Cooling profile of a Ti bar in an open-air benchtop environment. The black dots show the temperature decay measured experimentally, while the red line is an exponential model derived from Eq. (6), with the best linear fit, h = 13.

consumption levels. For each power level, there is an overlap between the values of $T_{\rm p}$ and the range $[T_{\rm m}(P_{\rm b}^{\rm min}), T_{\rm m}(P_{\rm b}^{\rm max})]$. As expected, higher power consumption levels led to a wider gap between the prototype's surface temperature and the room temperature, and this was consistently observed in both experimental and simulated data. Also note that higher power configurations drained the battery's voltage faster, which, in turn, widened the range of $T_{\rm m}$. Finally, we quantified the agreement between the experimental and simulation results by calculating the correlation coefficient between $T_{\rm p}$ and $T_{\rm m}$. Specifically, for each power level, we correlated the first and last value of $T_{\rm p}$ with $T_{\rm m}(P_{\rm b}^{\rm min})$ and $T_{\rm m}(P_{\rm b}^{\rm max})$, respectively, and obtained the correlation coefficient of 0.86 (p-value = 0.006).

Discussion

The thermal impact of fully-implantable BCI systems remains an under-researched topic [24]. Our CWU design in particular, and implantable BCIs in general (Fig. 1), bear some resemblance with commercially available IPGs. However, with an estimated range between 200 and 1600 μ W [65], IPGs' power consumption is about two orders of magnitude lower than that of implantable BCIs. This power gap is expected to be even larger for BD-BCIs. For this reason, we cannot assume that the thermal behavior of commercially available IPGs generalizes to fully-implantable BCIs.

To the best of our knowledge, this is the first thermal impact study of a CWU, envisioned as part of a fullyimplantable BD-BCI. Based on this study, we estimated



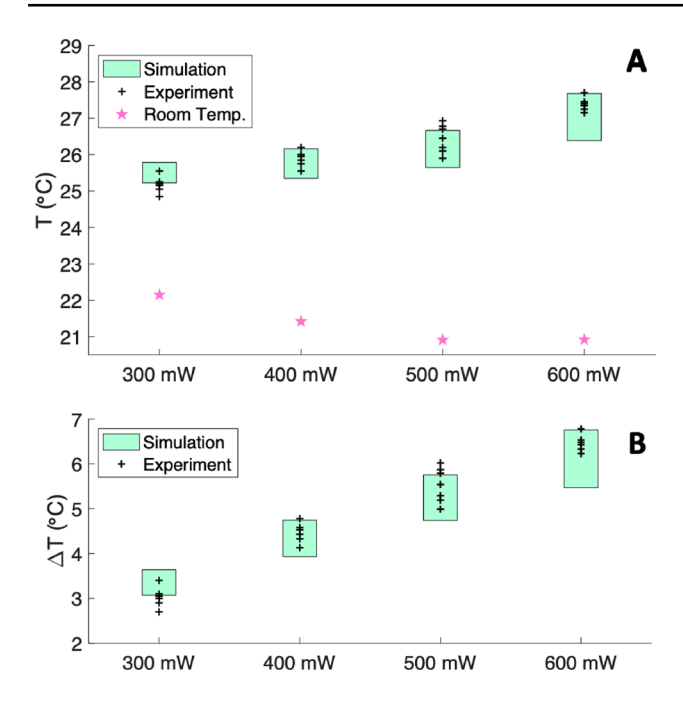


Fig. 8 The average top surface temperature of the thermal prototype in comparison to the simulated temperature range for different power consumption levels. (A) Actual temperature. (B) The same values expressed as a deviation from the room temperature. The black crosses are experimental temperature measurements, $T_{\rm p}$, repeated at ~ 10 -min intervals. The cyan boxes represent the simulated temperature range $[T_{\rm m}(P_{\rm b}^{\rm min}), T_{\rm m}(P_{\rm b}^{\rm max})]$. The pink stars show the average room temperature, $T_{\rm ext}$.

the CWU's maximum power budget that guarantees a thermally safe operation. Specifically, we simulated the bioheat model with nominal parameters, and we predicted that the CWU's power budget cannot exceed 458 mW without violating the 2° C thermal safety threshold. When perturbing 21 nominal parameters within their natural physiological and environmental range, 6 parameters had a negligible effect on the power budget. The remaining 15 parameters were critical and their simultaneous perturbation resulted in a power budget range between 378 and 538 mW. We believe that this power budget is sufficient for the CWU to perform its functions, such as training the decoder, online decoding, wireless communication and data transmission, and cortical stimulation. For example, our recently developed CWU benchtop prototype consumed on average 150 mW of power while performing all the BCI functions except stimulation [11]. Our newest BD-BCI benchtop prototype showed that cortical stimulation may require up to an additional 230 mW [12]. Taken together, these values suggest that the power budget range estimated based on our simulations is sufficient to power an actual CWU and likely a fully-implantable BD-BCI.

Our bio-heat modeling approach makes several simplifying assumptions. However, most of these assumptions

favored a more conservative power budget estimate, as described below. For example, we neglected the effects of radiative heat transfer. Since human skin is generally warmer than external room temperature, radiation would take heat away from the human body, and even more so when the CWU is powered. Therefore, the net effect of radiative heat transfer would be an even greater power budget. Another simplification of our approach is that we computed ΔT by comparing the temperature resulting from the active CWU simulation to a model where the CWU is inactive. An alternative way to define ΔT would be to compare the active simulation to a model where the CWU is not implanted. However, after comparing the two approaches, we conclude that the results presented here lead to a more conservative power budget estimate. However, after comparing our simulation results to those corresponding to a non-implant scenario, we conclude that the results presented here lead to a more conservative power budget estimate. Namely, in the absence of an implant, the fat and skin layers are closer to the body core and so their temperature is higher. This would, in turn, result in a lower value of ΔT and, therefore, would yield an even higher power budget. Furthermore, our model neglected external clothing. However, our worst-case scenario simulations assumed a 2-cm-thick wool layer and showed the effect of clothing on the power budget estimation to be minimal (< 2 mW). Additionally, we assumed a uniform electronics layer with thermal properties based on those of the PCB. Instead, a more detailed approach would be to split the electronics layer into the PCB and its electronic components (microcontroller core, H-bridge, current source, RAM module, NAND storage module, and radio TRX) [11, 12]. Given that the exact composition and arrangement of these components are currently unknown, we opted for a simpler approach. Once this information is known, such a detailed model could be used to rearrange the internal CWU components and further optimize the power budget. We also omitted a polymeric connection header that usually houses connectors and telemetry antenna in contemporary IPGs [27, 66]. However, since none of the elements in the header generate heat, we do not expect it to affect our power budget predictions. Additionally, the long-term heating of tissues can trigger adaptation mechanisms, such as angiogenesis, which increases blood perfusion and, in turn, reduces temperature. However, this process is poorly understood [67] and therefore could not be easily incorporated into our model. Finally, scar tissue encapsulation could occur around the CWU implant. When we repeated the simulations while encapsulating the CWU with 2-mm-thick scar tissue [68], the nominal power budget increased to from 458 to 519 mW. This power increase is due to the higher thermal conductivity of collagen compared to nearby tissues, which helps reduce the temperature surrounding the implant.



Table 4 shows that the thermal conductivity of fat and muscle, as well as the muscle blood perfusion, were the three most critical parameters of our bio-heat model, followed by the skin thickness and the fat and skin blood perfusion. This conclusion is consistent with the findings reported by in vivo animal studies [69]. Table 4 also shows that the perturbation of the same parameter across multiple tissues may or may not have the same effect on ΔT . For example, the increase of the fat's thickness led to a decrease in ΔT , while the increase of the muscle's thickness led to an increase in ΔT . (Note that from Eq. (5), it follows that both $S_i^+ > 0$ and $S_i^- < 0$ correspond to an increase in ΔT). For other parameters (e.g., blood perfusion), the perturbations in the same direction led to the same behavior across all tissues.

The main limitation of our study is the lack of in vivo validation. Nonetheless, FEM simulations are widely accepted in predicting active implants' behavior [20, 70–73]. This is especially true for preliminary studies, where it would be both unethical and cost ineffective to perform animal testing. Once an active implant prototype has been finalized, animal studies are appropriate to test both its function and safety. These include long-term functional tests and FDA safety requirements, such as thermal impact, biocompatibility, and current leakage (ISO 14708-1). Additionally, the risks associated with prolonged exposure to mild heat due to the CWU implant can raise concerns. However, given that similar devices, such as DBS [20], have been shown to be safe even when operating continuously for years, we expect the CWU implant, which will operate intermittently, to be safe as well.

In the absence of animal testing, we used a benchtop model to validate the general FEM approach presented here. For this model, the simulation results overlapped with the experimental results for all power configurations (see Fig. 8), and therefore we conclude that the FEM reliably predicts experimental thermal behavior. The differences between the experimental and simulation results can be attributed to the model's simplifying assumptions. First, the model assumed constant parameters, like $T_{\rm ext}$ and h. However, these parameters could have changed during the course of experiments due to sudden fluctuations in room temperature and air flow, caused by external factors (door opening/closing, A/C turning on/off). Additionally, the benchtop simulation omitted smaller components, like the cables, switches and connector; however, we do not expect these elements to have a great influence on the heat distribution. Lastly, observational errors from the experimental measurements could also have been a source of discrepancy.

Our estimated power budget range (378 to 538 mW) provides an informative constraint for the future design of a fully-implantable CWU and a BD-BCI system, as outlined in Fig. 1. This study focuses on the thermal analysis of the CWU because it is the most power-hungry component of the

BD-BCI system. Other heat-dissipating components include the skull unit (SU) and sensory (stimulating) electrodes. Our preliminary power budget estimates for the SU are provided in [22], and efforts to incorporate the stimulating electrodes into this model are currently under way. Nevertheless, to ultimately validate the thermal safety of these components, in vivo animal testing must be done. However, animal testing is out of the scope of this work and will be pursued in our future studies, where the CWU and other components of the BD-BCI system will be implanted in a large animal model. Specifically for the CWU, a temperature sensor (e.g., thermistor) can be integrated within the implant to continuously measure its surface temperature at the hottest region. Note that this temperature is equal to the temperature of the adjacent tissues due to temperature continuity (see Fig. 5). The CWU's wireless communication system could be exploited to obtain periodic measurements of the CWU's surface temperature. To validate the thermal safety of the device, its thermal impact can be assessed under different power consumption levels (generated by different operation modalities) and ensure that the 2°C threshold is not violated under any circumstances.

Funding This work was supported by the National Science Foundation (Award No. 1646275). Claudia Serrano-Amenos also acknowledges the support from the Balsells Fellowship.

Declarations

Conflict of interest No benefits in any form have been or will be received from a commercial party related directly or indirectly to the subject of this manuscript.

References

- Arzuaga, P. Cardiac pacemakers: Past, present and future. IEEE Instrumentation and Measurement Magazine. 17(3):21–27, 2014.
- DiMarco, J. P. Implantable cardioverter-defibrillators. New England Journal of Medicine. 349(19):1836–1847, 2003.
- George, M. S., H. A. Sackeim, A. J. Rush, L. B. Marangell, Z. Nahas, M. M. Husain, S. Lisanby, T. Burt, J. Goldman, and J. C. Ballenger. Vagus nerve stimulation: A new tool for brain research and therapy. *Biological Psychiatry*. 47(4):287–295, 2000.
- Lozano, A. M., N. Lipsman, H. Bergman, P. Brown, S. Chabardes, J. W. Chang, K. Matthews, C. C. McIntyre, T. E. Schlaepfer, M. Schulder, Y. Temel, J. Volkmann, and J. K. Krauss. Deep brain stimulation: Current challenges and future directions. *Nature Reviews Neurology*. 15(3):148–160, 2019.
- Morrell, M. J. Responsive cortical stimulation for the treatment of medically intractable partial epilepsy. *Neurology*. 77(13):1295– 1304, 2011.
- Dewhirst, M. W., B. L. Viglianti, M. Lora-Michiels, M. Hanson, and P. J. Hoopes. Basic principles of thermal dosimetry and thermal thresholds for tissue damage from hyperthermia. *Interna*tional Journal of Hyperthermia. 19(3):267–294, 2003.



- A. Mahajan, A. K. Bidhendi, P. T. Wang, C. M. McCrimmon, C. Y. Liu, Z. Nenadic, A. H. Do, and P. Heydari. A 64-channel ultra-low power bioelectric signal acquisition system for braincomputer interface. In: *IEEE biomedical circuits and systems con*ference: engineering for healthy minds and able bodies, BioCAS 2015 - Proceedings, pp. 3–6, 2015.
- Karimi-Bidhendi, A., O. Malekzadeh-Arasteh, M. C. Lee, C. M. McCrimmon, P. T. Wang, A. Mahajan, C. Yu Liu, Z. Nenadic, A. H. Do, and P. Heydari. CMOS ultralow power brain signal acquisition front-ends: Design and human testing. *IEEE Transactions on Biomedical Circuits and Systems*. 11(5):1111–1122, 2017.
- O. Malekzadeh-Arasteh, H. Pu, J. Lim, C. Y. Liu, A. H. Do, Z. Nenadic, and P. Heydari. An energy-efficient CMOS dual-mode array architecture for high-density ECoG-based brain-machine interfaces. In: *IEEE transactions on biomedical circuits and sys*tems, pp. 1–11, 2019.
- Lee, M. C., A. Karimi-Bidhendi, O. Malekzadeh-Arasteh, P. T. Wang, A. H. Do, Z. Nenadic, and P. Heydari. A CMOS MedRadio transceiver with supply-modulated power saving technique for an implantable brain-machine interface system. *IEEE Journal of Solid-State Circuits*. 54(6):1541–1552, 2019.
- Wang, P. T., E. Camacho, M. Wang, Y. Li, S. J. Shaw, M. Armacost, H. Gong, D. Kramer, B. Lee, R. A. Andersen, C. Y. Liu, P. Heydari, Z. Nenadic, and A. H. Do. A benchtop system to assess the feasibility of a fully independent and implantable brainmachine interface. *Journal of Neural Engineering*. 16(6):066043, 2019.
- Sohn, W. J., J. Lim, P. T. Wang, H. Pu, O. Malekzadeh-Arasteh, S. J. Shaw, M. Armacost, H. Gong, S. Kellis, R. A. Andersen, C. Y. Liu, P. Heydari, Z. Nenadic, and A. H. Do. Benchtop and bedside validation of a low-cost programmable cortical stimulator in a testbed for bi-directional brain-computer-interface research. Frontiers in Neuroscience. 16:1075971, 2023.
- 13. T. Campi, S. Cruciani, V. De Santis, and M. Feliziani. EMF safety and thermal aspects in a pacemaker equipped with a wireless power transfer system working at low frequency. In: *IEEE transactions on microwave theory and techniques*, pp. 1–8, 2016.
- Mohsin, S. A. Concentration of the specific absorption rate around deep brain stimulation electrodes during MRI. *Progress In Electromagnetics Research*. 121:469–484, 2011.
- Winter, L., F. Seifert, L. Zilberti, M. Murbach, and B. Ittermann. MRI-related heating of implants and devices: A review. *Journal of Magnetic Resonance Imaging*. 53(6):1646–1665, 2021.
- Kim, J., and Y. Rahmat-Samii. Implanted antennas inside a human body: Simulations, designs, and characterizations. *IEEE Transac*tions on Microwave Theory and Techniques. 52(8):1934–1943, 2004
- Narayanamoorthi, R. Modeling of capacitive resonant wireless power and data transfer to deep biomedical implants. *IEEE Trans*actions on Components, Packaging and Manufacturing Technology. 9(7):1253–1263, 2019.
- Ibrahim, T. S., D. Abraham, and R. L. Rennaker. Electromagnetic power absorption and temperature changes due to brain machine interface operation. *Annals of Biomedical Engineering*. 35(5):825–834, 2007.
- Sohee, K., P. Tathireddy, R. A. Normann, and F. Solzbacher. Thermal impact of an active 3-D microelectrode array implanted in the brain. *IEEE Transactions on Neural Systems and Rehabilitation Engineering*. 15(4):493–501, 2007.
- Elwassif, M. M., Q. Kong, M. Vazquez, and M. Bikson. Bio-heat transfer model of deep brain stimulation-induced temperature changes. *Journal of Neural Engineering*. 3(4):306, 2006.
- Opie, N. L., A. N. Burkitt, H. Meffin, and D. B. Grayden. Heating of the eye by a retinal prosthesis: Modeling, cadaver and in vivo

- study. *IEEE Transactions on Biomedical Engineering*. 59(2):339–345, 2012.
- C. Serrano-Amenos, F. Hu, P. T. Wang, S. Kellis, R. A. Andersen, C. Y. Liu, P. Heydari, A. H. Do, and Z. Nenadic. Thermal analysis of a skull implant in brain-computer interfaces. In 2020 42nd Annual international conference of the IEEE engineering in medicine biology society (EMBC), pp. 3066–3069, 2020.
- Serrano-Amenos, C., P. Heydari, C. Y. Liu, A. H. Do, and Z. Nenadic. Power budget of a skull unit in a fully-implantable braincomputer interface: Bio-heat model. *Transactions on neural sys*tems and rehabilitation engineering. 31:4029–4039, 2023.
- Wolf, P. D. Thermal considerations for the design of an implanted cortical brain-machine interface (BMI). In: Indwelling neural implants: Strategies for contending with the in vivo environment, edited by W. M. Reichert. Boca Raton: CRC Press/Taylor & Francis, 2008, pp. 1–20.
- Rizk, M., I. Obeid, S. H. Callender, and P. D. Wolf. A singlechip signal processing and telemetry engine for an implantable 96-channel neural data acquisition system. *Journal of Neural Engineering*. 4(3):309, 2007.
- Haghjoo, M. Techniques of permanent pacemaker implantation, current issues and recent advances in pacemaker therapy. *Cardiovascular Medicine*. 1:4–10, 2012.
- Sarica, C., C. Iorio-Morin, D. H. Aguirre-Padilla, A. Najjar, M. Paff, A. Fomenko, K. Yamamoto, A. Zemmar, N. Lipsman, G. M. Ibrahim, C. Hamani, M. Hodaie, A. M. Lozano, P. M. Renato, A. Fasano, and S. K. Kalia. Implantable pulse generators for deep brain stimulation: Challenges, complications, and strategies for practicality and longevity. Frontiers in Human Neuroscience. 15:7084–2021
- Laurent, A., F. Mistretta, D. Bottigioli, K. Dahel, C. Goujon, J. F. Nicolas, A. Hennino, and P. E. Laurent. Echographic measurement of skin thickness in adults by high frequency ultrasound to assess the appropriate microneedle length for intradermal delivery of vaccines. *Vaccine*. 25(34):6423–6430, 2007.
- Störchle, P., W. Müller, M. Sengeis, S. Lackner, S. Holasek, and A. Fürhapter-Rieger. Measurement of mean subcutaneous fat thickness: Eight standardised ultrasound sites compared to 216 randomly selected sites. *Scientific Reports*. 8(1):16268, 2018.
- Bueno, A. F., F. A. Lemos, M. E. Ferrareze, W. A. M. dos Santos, F. V. Veronese, and A. S. Dias. Muscle thickness of the pectoralis major and rectus abdominis and level of physical activity in chronic hemodialysis patients. *Jornal Brasileiro de Nefrologia*. 39(4):391, 2017.
- Mohr, M., E. Abrams, C. Engel, W. B. Long, and M. Bottlang. Geometry of human ribs pertinent to orthopedic chest-wall reconstruction. *Journal of Biomechanics*. 40(6):1310–1317, 2007.
- Sette, A. L., E. Seigneuret, F. Reymond, S. Chabardes, A. Castrioto, B. Boussat, E. Moro, P. François, and V. Fraix. Battery longevity of neurostimulators in Parkinson disease: A historic cohort study. *Brain Stimulation*. 12(4):851–857, 2019.
- 33. Pennes, H. H. Analysis of tissue and arterial blood temperatures in the resting human forearm. *Journal of Applied Physiology*. 1(2):93–122, 1948.
- 34. Duck, F. A. Thermal properties of tissue. In: Physical properties of tissues, Amsterdam: Elsevier, 1990, pp. 9–42.
- Gordon, R. G., R. B. Roemer, and S. M. Horvath. A mathematical model of the human temperature regulatory system-transient cold exposure response. *IEEE Transactions on Biomedical Engineer*ing. BME–23(6):434–444, 1976.
- Wang, Z., Z. Ying, A. Bosy-Westphal, J. Zhang, B. Schautz, W. Later, S. B. Heymsfield, and M. J. Müller. Specific metabolic rates of major organs and tissues across adulthood: Evaluation by mechanistic model of resting energy expenditure. *The American Journal of Clinical Nutrition*. 92(6):1369–1377, 2010.



- Heinonen, I., M. Bucci, J. Kemppainen, J. Knuuti, P. Nuutila, R. Boushel, and K. K. Kalliokoski. Regulation of subcutaneous adipose tissue blood flow during exercise in humans. *Journal of Applied Physiology*. 112(6):1059–1063, 2012.
- 38. Heinonen, I., R. Boushel, Y. Hellsten, and K. Kalliokoski. Regulation of bone blood flow in humans: The role of nitric oxide, prostaglandins, and adenosine. *Scandinavian Journal of Medicine & Science in Sports*. 28(5):1552–1558, 2018.
- Workman, J. M., and B. W. Armstrong. Oxygen cost of treadmill walking. *Journal of Applied Physiology*, 18(4):798–803, 1963.
- Grimby, G., E. Häggendal, and B. Saltin. Local xenon 133 clearance from the quadriceps muscle during exercise in man. *Journal* of Applied Physiology. 22(2):305–310, 1967.
- Kovacs, G., A. Berghold, S. Scheidl, and H. Olschewski. Pulmonary arterial pressure during rest and exercise in healthy subjects: A systematic review. *European Respiratory Journal*. 34(4):888–894, 2009.
- Argiento, P., N. Chesler, M. Mule, M. D'Alto, E. Bossone, P. Unger, and R. Naeije. Exercise stress echocardiography for the study of the pulmonary circulation. *European Respiratory Journal*. 35(6):1273– 1278, 2010.
- Lee, S. M. C., W. J. Williams, and S. M. Schneider. Role of skin blood flow and sweating rate in exercise thermoregulation after bed rest. *Journal of Applied Physiology*, 92(5):2026–2034, 2002.
- Guyton, A. C. Human physiology and mechanisms of disease, 6th ed. London: W B Saunders, 1996.
- Barrett, K. E., S. M. Barman, J. Yuan, and H. L. Brooks. Ganong's review of medical physiology, 26th ed. McGraw-Hill Education/ Medical, 2019.
- Mapleson, W. W. An electric analogue for uptake and exchange of inert gases and other agents. *Journal of Applied Physiology*. 18(1):197–204, 1963.
- Cowles, A. L., H. H. Borgstedt, and A. J. Gillies. Tissue weights and rates of blood flow in man for the prediction of anesthetic uptake and distribution. *Anesthesiology*. 35(5):523–526, 1971.
- Williams, L. R., and R. W. Leggett. Reference values for resting blood flow to organs of man. *Clinical Physics and Physiological Measurement*. 10(3):187–217, 1989.
- McIntosh, R. L., and V. Aderson. A comprehensive tissue properties database provided for the thermal assessment of a human at rest. *Biophysical Reviews and Letters*. 05(03):129–151, 2010.
- Powell, R. W., and R. P. Tye. The thermal and electrical conductivity of titanium and its alloys. *Journal of the Less-Common Metals*. 3(3):226–233, 1961.
- Beirão, S. G. S., A. P. Ribeiro, M. J. Lourenço, F. J. V. Santos, and C. A. Nieto De Castro. Thermal conductivity of humid air. *International Journal of Thermophysics*. 33(8–9):1686–1703, 2012.
- S. P. Gurrum, D. R. Edwards, T. Marchand-Golder, J. Akiyama, S. Yokoya, J. F. Drouard, and F. Dahan. Generic thermal analysis for phone and tablet systems. In 2012 IEEE 62nd electronic components and technology conference, pp. 1488–1492. IEEE, 2012.
- 53. Nirale, V. Evaluation of effective thermal conductivity in PCB. *IJRST*. 3:174–179, 2016.
- Kosky, P., R. Balmer, W. Keat, and G. Wise. Mechanical engineering. In: Exploring engineering, Amsterdam: Elsevier, 2021, pp. 317–340.
- Del Bene, V. E. Temperature. In: Clinical methods: The history, physical, and laboratory examinations, Boston: Butterworths, 1990.
- Best, C. H., N. B. Taylor, and J. R. Brobeck. Best & Taylor's physiological basis of medical practice. Williams & Wilkins, 1979.
- Downing, D. J., R. H. Gardner, and F. O. Hoffman. An examination of response-surface methodologies for uncertainty analysis in assessment models. *Technometrics*. 27(2):151–163, 1985.

- Lazzi, G. Thermal effects of bioimplants. *IEEE Engineering in Medicine and Biology Magazine*. 24(5):75–81, 2005.
- Yao, C., J. Lu, and T. J. Webster. Titanium and cobalt-chromium alloys for hips and knees. In: Biomaterials for artificial organs, edited by M. Lysaght, and T. J. Webster. Amsterdam: Elsevier, 2011, pp. 34–55.
- Boyer, R., G. Welsch, and E. W. Collings. Materials properties handbook - titanium alloys. ASM International, 1994.
- Seo, J., J. Jeon, J.-H. Lee, and S. Kim. Thermal performance analysis according to wood flooring structure for energy conservation in radiant floor heating systems. *Energy and Buildings*. 43(8):2039–2042, 2011
- Ohmite. Characteristics for ohmite axial-leaded resistor materials. https://www.ohmite.com/axial-resistors-material-characteristics/. Accessed: 2022-12-06.
- Technical Products, Inc. https://www.technicalproductsinc.com. Accessed: 2022-12-06.
- 64. Desai, P. D. Thermodynamic properties of titanium. *International Journal of Thermophysics*. 8(6):781–794, 1987.
- Cubo, R., M. Fahlström, E. Jiltsova, H. Andersson, and A. Medvedev. Calculating deep brain stimulation amplitudes and power consumption by constrained optimization. *Journal of Neural Engi*neering. 16(1):016020, 2019.
- R. B. Strother, G. B. Trophe, J. J. Mrva, and D. R. Pack. Implantable pulse generator systemis and methods for providing functional and/ or therapeute stmulation of muscles and/or nerves and/or central nervous system tissue, 2007.
- Davies, C. R., F. Fukumura, K. Fukamachi, K. Muramoto, S. C. Himley, A. Massiello, J.-F. Chen, and H. Harasaki. Adaptation of tissue to a chronic heat load. *ASAIO Journal*. 40(3):M514–M517, 1994.
- 68. D. Do. personal communication.
- Okazaki, Y., C. R. Davies, T. Matsuyoshi, K. Fukamachi, K. E. Wika, and H. Harasaki. Heat from an implanted power source is mainly dissipated by blood perfusion. *ASAIO Journal American* Society for Artificial Internal Organs. 43(5):585–588, 1997.
- Matsuki, H., T. Matsuzaki, and T. Satoh. Simulations of temperature rise on transcutaneous energy transmission by non-contact energy transmitting coils. *IEEE Transactions on Magnetics*. 29(6):3334– 3336, 1993.
- Walckiers, G., B. Fuchs, J.-P. Thiran, J. R. Mosig, and C. Pollo. Influence of the implanted pulse generator as reference electrode in finite element model of monopolar deep brain stimulation. *Journal* of Neuroscience Methods. 186(1):90–96, 2010.
- Yousif, N., and X. Liu. Investigating the depth electrode-brain interface in deep brain stimulation using finite element models with graded complexity in structure and solution. *Journal of Neurosci*ence Methods. 184(1):142–151, 2009.
- Pelot, N. A., B. J. Thio, and W. M. Grill. Modeling current sources for neural stimulation in COMSOL. Frontiers in Computational Neuroscience. 12:40, 2018.

Publisher's Note Springer Nature remains neutral with regard to jurisdictional claims in published maps and institutional affiliations.

Springer Nature or its licensor (e.g. a society or other partner) holds exclusive rights to this article under a publishing agreement with the author(s) or other rightsholder(s); author self-archiving of the accepted manuscript version of this article is solely governed by the terms of such publishing agreement and applicable law.

